Archive of Applied Mechanics manuscript No.
(will be inserted by the editor)

The effect of vertical ground movement on masonry walls simulated through an elastic-plastic interphase meso-model: a case study.

Antonino Spada

Received: date / Accepted: date

Abstract The present paper proposes an interphase model for the simulation of damage propagation in masonry walls in the framework of a mesoscopic approach. The model is thermodynamically consistent, with constitutive relations derived from a Helmholtz free potential energy. With respect to classic interface elements the internal stress contribute is added to the contact stresses. It is considered that damage, in the form of loss of adhesion or cohesion, can potentially take place at each of the two blocks-mortar physical interfaces. Flow rules are obtained in the framework of the Theory of Plasticity, considering bilinear domains of 'Coulomb with tension cut-off' type. The model aims to be a first research step to solve the inverse problem of damage propagation in masonry generated by vertical ground movements, in order to ex-post identify the cause of a visible damage. The constitutive model is written in a discrete form for its implementation in a research-oriented finite element program. The response at the quadrature point is analyzed first. Then, the model is validated through comparisons with experimental results and finally employed to simulate the failure occurred in a wall of an ancient masonry building, where an arched collapse took place due to a lowering of the ground level under part of its foundation.

Keywords masonry · interphase model · ground movement · foundation settlement · finite elements

1 Introduction

Masonry is one of the most ancient building techniques, extensively used all around the world thanks to the possibility to obtain its basic constituents starting from local raw materials. A great number of historical buildings are masonry structures, often constituting the world cultural heritage, located in residential zones and even in seismic areas.

Antonino Spada
DICAM - University of Palermo - Viale delle Scienze, Ed. 8
Tel.: +39-091-238-96723 - Fax: +39-091-427121
E-mail: antonino.spada@unipa.it

Since it is known that masonry is a quasi-brittle material which easily suffers the consequences of external actions, a big effort was done in the past to better understand its mechanical behavior. Even today this effort continues in order to find the most efficient strategy which best reproduces masonry response to the most common boundary conditions. The complexity of the problem and the continuous need to preserve historical buildings from natural events or human tendency to renew residential areas make this topic still now an open field. The necessity to find relatively quick answers to specific situations encourages many researches to join discussions and furnish sophisticated numerical models able to reproduce each single problem compatibly with the power of actual calculators.
Despite cracks in masonry can be caused, from a structural point of view, by either the behavior of its constituents (mortar shrinkage, brick expansion, brick-mortar compatibility, etc.) or a modification of the structural arrangement (that leads in some cases to a dangerous redistribution of stresses), the main cause of masonry failure is due to ground movements. It is possible to distinguish between horizontal and vertical movements, the former mainly derived by seismic actions or landslides, the latter connectable with soil consolidation and foundation settlement, ground subsidence, tunneling-induced deformations.
The existing numerical models can be divided into three main groups: models in which the building, the ground and any action on the ground are combined in a single numerical model; models in which the building is analyzed by including the effects of the soil-structure interaction; models in which the building only is analyzed under specific boundary conditions. If the model is used to simulate qualitatively the overall behavior of a structure on the basis of a modification in a specific area of the ground, then the models of the first group are the best ones. If the desired answer requires a detailed outcome for the structure, the third type is the most suitable, since more accurate analyzes can be conducted on the single building or part of it.
The majority of the papers investigating damage caused by vertical movements at the base of masonry structures concentrate on the problems of foundation settlement or settlement caused by tunneling. The first problem arises anytime a new construction is built, especially on unconsolidated soils. The second problem is deeply felt during excavation for underground facilities, mining, or deep foundations in urban areas.
An extended investigation on the tunneling-induced settlement of masonry buildings was made by Houlsby and his group: a 2D finite element (FE) analysis on a masonry facade including its interaction with soil was performed by Liu et al. [23] considering an elastoplastic behavior for the soil and an elastic no-tension model for masonry; a complete 3D FE model in which tunnel, soil and building are all treated in a single analysis was presented in Burd et al [9]; the same 3D model was studied by Augarde and Burd [6] discussing the advantages of using shell or tetrahedral continuum elements for lined tunnels.
In all these previous works simple damage models were employed for the structure. However, new numerical studies performed by Son and Cording [35] demonstrated that the structural response to excavation-induced ground movements is highly dependent on both cracking in the structure and structural type. This was confirmed by Truong-Hong and Laefer [38]. By employing a smeared crack model for masonry, they analyzed 16 FE models on masonry walls subjected to excavation-induced settlements, to investigate the impact on the building response of 3 par-

ticular window shapes, window size and brick orientation.
Netzel and Ziji [28] studied solid masonry walls where the soil-structure interaction was modeled through an elastic-perfectly plastic interface and the structure as an anisotropic continuum material with a Rankine-Hill behavior. Giardina et al. [20] used a semi-coupled approach to develop a 2D FE model with settlements applied to a non-linear interface to simulate the soil-structure interaction and masonry treated as a single material with homogenized properties and smeared damage. A similar approach was followed by Amorosi et al. [5] for application to a real structure (the Felice aqueduct in Rome). They simulated the structure as a homogenized anisotropic continuum in plane stress conditions (whose constitutive relations were derived from masonry with a periodic texture), and the soil as a linear elastic-perfectly plastic material where Gaussian-type displacements were imposed.
Galassi et al. [12] chose a different way to simulate the non-linear behavior of masonry. They imagined masonry as a system of rigid blocks connected by no-tension resistant frictional links and simulated damage propagation in arches and trabs of the Pompeianus Forum (Naples) by imposing external settlements.
A larger interest towards more accurate damage propagation in masonry took place in the last years, thanks to the great progress in Continuum Damage Mechanics, Theory of Plasticity, and Fracture Mechanics. Many of these models are validated on laboratory tests only, and not so much works show results on real structures. A wide numerical investigation was performed by Alessandri et al. [3] to solve an inverse problem in order to identify the location and the entity of the settlement in the Palazzo Gulinelli (Ferrara). The numerical survey was performed through 2D and 3D nonlinear FE analyses employing different material behaviors and a Mohr-Coulomb criterion for masonry failure. The authors highlighted the importance to correctly identify and quantify settlements provoking visible crack patterns, in order to establish the most correct intervention of rehabilitation.
A 3D rigid block limit analysis using a Mohr-Coulomb type point-contact formulation was used by Portioli and Cascini [31]. An inverse problem to predict fracture patterns in masonry structures produced by imposed settlements or distortions with application to two reals structures is lately faced by Iannuzzo et al. [21]. They simulated the structure as a Heyman simplified masonry model looking for the minimum potential energy of the structure for given piecewise rigid displacements.
Except some of the latest works, most of the cited papers treat masonry as a homogeneous material in the framework of a macroscopic approach. In the macroscopic approach, constitutive laws are expressed in terms of macroscopic stress and average strain for the equivalent continuum. This approach permits to obtain more or less good results depending on the complexity of the averaging process and sometimes it fails in the proper masonry description since the specific interaction between elements is not taken into consideration. Other two alternative approaches have been studied: the mesoscopic approach and the multiscale approach. The mesoscopic approach is the best existing method for the description of damage propagation in masonry. It considers masonry as a heterogeneous material made of blocks and mortar, which are individually modeled. Since masonry presents a mechanical response strongly dependent on the inelastic phenomena occurring at the joints, a common strategy is to substitute mortar joints with non-linear mechanical devices called zero-thickness interface/interphase elements.

In such elements the inelastic phenomena are properly described starting from the displacement discontinuities between the two blocks in contact. Many examples of interface/interphase application to masonry can be found in literature. The most recent ones are mentioned in the following.
Lofti and Shing [24] and Lourenço and Rots [25] proposed interface models in the framework of plasticity for non-standard materials and fracture mechanics adopting Mohr-Coulomb type failure criteria. Giambanco et al. [15] proposed a similar model, focusing on the cohesive-frictional joint transition and taking into account the effect of geometrical dilatancy. Giambanco and Fileccia Scimemi [13] developed a time-dependent interface in the framework of viscoplasticity. Alfano and Sacco [4], Parrinello et al. [29], Spada et al. [36] combined damage and plasticity considering the contact area divided in a fully damaged part and an undamaged part, with a sort of phase transition occurring on the basis of damage propagation and inelastic strains taking place when the stress level violated appropriate elastic-plastic domains. A combined finite-discrete element method allowing fragmentation of masonry walls was introduced by Smoljanović et al. [34], while a comparison between discrete models and discrete-finite element models was furnished by Baraldi et al. [7].
The enhancement of the interface elements is represented by the interphase elements. The novelty introduced by these models resides in the addition of internal stresses to the contact tractions of the interface models. After the pioneering work of Giambanco and Mróz [14] and the implementation in the framework of finite elements by Giambanco et al. [16], some application to masonry material appeared in the last years. Fileccia Scimemi et al. [11] developed an interphase model where damage in the joint material is described separately from the loss of adhesion at the joint-adherent contact surface. Addessi and Sacco [2] proposed a kinematic enriched model for the analysis of masonry subjected to in-plane loading conditions using a damage-friction failure criterion based on an extension of the Mohr-Coulomb law for mortar joints. A soft interface comprising large displacements and evolving microcraking was introduced as an interphase model by Raffa et al. [32]. Serpieri et al. [33] finally worked with a 3D interphase formulation to reproduce crack formation and relative frictional and dilatancy effects in masonry panels.
In the last decades great attention has been paid to the multiscale approach, whose virtues and vices are still nowadays debated. This technique consists in performing numerical analyses coupling two different scales, by employing apposite transition laws. At the macroscale the structure is treated as a homogeneous continuum whose constitutive behavior is determined 'on the fly' by solving a mesoscale boundary value problem. Multiscale models are commonly divided in two groups. In the first order methods the Cauchy model is used at both scales: usually FEs are employed at both scales and periodic boundary conditions at the mesoscale ([22, 26, 27, 30]). Alternatively, the Meshless method and linear boundary conditions have been proposed ([17, 19, 37]). In the second order methods Cosserat or higher order continua are used, when strong strain and stress gradients arise at the macroscale ([1]).
The present paper builds on the works of Giambanco and Mróz [14], Giambanco et al. [16], Fileccia Scimemi et al. [11], and propose an interphase model with the specific aim to solve the inverse problem in real cases with damage patterns generated by vertical ground movements, in order to ex-post look for the cause

of a visible damage. The basic kinematic assumptions of the interphase model are furnished by Giambanco and Mróz [14] and are here reported in Section 2 for the sake of completeness. A simpler constitutive model is proposed with respect to that one developed by Fileccia Scimemi et al. [11]. Even if for certain aspects the two models are similar, they differ in two key points. First, inelasticity is assumed potentially developing on two separate surfaces rather than a unique, collapsed middle surface. Second, damage effects related to internal stresses are neglected, living their insertion for eventual future developments. The main idea is based on the assumption that ancient masonry presents poor quality of mortar, with strongly reduced values of cohesion and adhesion at the mortar-block physical interfaces, where usually detachments take place. For this reason, although a coupled plastic-damage formulation would always give a more refined response (but a harder formulation and implementation), a plasticity model only is considered sufficient to catch the qualitatively correct collapse mechanism. It is in fact remarkable to note that the calibration of damage parameters is not easy if not supported by specific laboratory tests. The possibility to obtain the correct behavior using only plasticity has also been shown by Giambanco and Di Gati [18], translating the activation domain in the displacement space.
The proposed model is thermodynamically consistent. Flow rules are written in the framework of the Theory of Plasticity, considering bilinear domains of the 'Coulomb with tension cut-off' type. The model was implemented in a research-oriented FE analysis program able to run numerical analyses within the mesoscopic approach, but it can be potentially incorporated in programs where the soil-structure interaction is also taken into account. Regarding the quadrature rule of the finite element, the Selective Reduced Integration (SRI) scheme showed in Giambanco et al. [16] was applied. The soundness of the model is showed analyzing its behavior at quadrature point and reproducing experimental results on masonry panels available in literature. A case-study on a wall of a real ancient masonry building where a failure clearly took place due to the vertical movement of part of its foundation is also shown. The latter could be considered as the main novelty point of the paper.
The paper is organized as follows. In Section 2 the interphase concept is recalled. In Section 3 the interphase constitutive model is presented, while in Section 4 its discrete formulation is furnished. Section 5 shows the performance of a single interphase element when subjected to simple and mixed modes. In Section 6 the model is validated showing the comparison between numerical results and experimental data by Portioli and Cascini [31]. In Section 7 the model is applied to solve the case of 'Baglio Granatelli' (Trapani). Conclusions and future developments are finally reported in Section 8.

2 The interphase concept

Let us consider, in the Euclidean space $\Re^3$, a system formed by two adherents Ω^+ and Ω^- connected by a third weak body whose thickness h is small with respect to other dimensions. With reference to Fig. 1a, where a local $x - z$ view of the system is depicted, Σ^+ and Σ^- identify two physical interfaces through which the weak body of volume V interacts with the two adherents, exchanging the tractions $\mathbf{t}^+$ and $\mathbf{t}^-$ respectively, as shown in Fig. 1b. The tractions $\mathbf{t}^+$ and $\mathbf{t}^-$ can be

considered as external actions for the third body, whose stress state is completely defined by the indicated σ_x, σ_z and τ_{xz} components, under the hypothesis of plane stress conditions. In Fig. 1b $\mathbf{n}^+$, $\mathbf{s}^+$, $\mathbf{n}^-$, $\mathbf{s}^-$ identify the normal and tangential unit vectors to the Σ^+ and Σ^- surfaces respectively.
The weak body can be regarded as an *interphase model*, where the fibers directed along the normal to the middle surface Σ are maintained rectilinear along the deformation process [14]. This hypothesis permits to define the displacement field $\mathbf{u}$ in the interphase, once the displacements $\mathbf{u}^+$ and $\mathbf{u}^-$ in Σ^+ and Σ^- are respectively known:

$$\mathbf{u}(x,y,z) = \left(\frac{1}{2} + \frac{z}{h}\right)\mathbf{u}^+(x,y) + \left(\frac{1}{2} - \frac{z}{h}\right)\mathbf{u}^-(x,y)\,. \tag{1}$$

where y identifies the third direction of the local reference system.
The correspondent strain field is classically obtained by applying the compatibility matrix $\mathbf{C}$ on the displacement field $\mathbf{u}$, thus:

$$\begin{aligned}\boldsymbol{\varepsilon}(x,y,z) = \mathbf{C}\mathbf{u}(x,y,z) = \\ = \mathbf{C}\left[\left(\frac{1}{2} + \frac{z}{h}\right)\mathbf{u}^+(x,y)\right] + \mathbf{C}\left[\left(\frac{1}{2} - \frac{z}{h}\right)\mathbf{u}^-(x,y)\right].\end{aligned} \tag{2}$$

Assuming a uniform strain over the thickness of the joint, due to its smallness with respect to other two dimensions, we have:

$$\begin{aligned}\hat{\boldsymbol{\varepsilon}}(x,y) = \frac{1}{h}\int_{-h/2}^{h/2}\boldsymbol{\varepsilon}(x,y,z)dz = \frac{1}{2h}\int_{-h/2}^{h/2}\mathbf{C}\left[\mathbf{u}^+(x,y) + \mathbf{u}^-(x,y)\right]dz + \\ + \frac{1}{h^2}\int_{-h/2}^{h/2}\left(z\,\tilde{\mathbf{C}} + \tilde{\mathbf{C}}_n\right)\left[\mathbf{u}^+(x,y) - \mathbf{u}^-(x,y)\right]dz,\end{aligned} \tag{3}$$

where $\hat{\boldsymbol{\varepsilon}}$ represents the mean value of the strain over the thickness of the joint. The three compatibility matrices can be explicitly written as:

$$\mathbf{C} = \begin{bmatrix} \frac{\partial}{\partial x} & 0 & 0 \\ 0 & \frac{\partial}{\partial y} & 0 \\ 0 & 0 & \frac{\partial}{\partial z} \\ \frac{\partial}{\partial y} & \frac{\partial}{\partial x} & 0 \\ \frac{\partial}{\partial z} & 0 & \frac{\partial}{\partial x} \\ 0 & \frac{\partial}{\partial z} & \frac{\partial}{\partial y} \end{bmatrix} \qquad \tilde{\mathbf{C}} = \begin{bmatrix} \frac{\partial}{\partial x} & 0 & 0 \\ 0 & \frac{\partial}{\partial y} & 0 \\ 0 & 0 & 0 \\ \frac{\partial}{\partial y} & \frac{\partial}{\partial x} & 0 \\ 0 & 0 & \frac{\partial}{\partial x} \\ 0 & 0 & \frac{\partial}{\partial y} \end{bmatrix} \qquad \tilde{\mathbf{C}}_n = \begin{bmatrix} 0 & 0 & 0 \\ 0 & 0 & 0 \\ 0 & 0 & 1 \\ 0 & 0 & 0 \\ 1 & 0 & 0 \\ 0 & 1 & 0 \end{bmatrix}. \tag{4}$$

By solving the integrals of Eq. (3) a more compact expression is obtained for $\hat{\boldsymbol{\varepsilon}}$, that is:

$$\hat{\boldsymbol{\varepsilon}}(x,y) = \frac{\mathbf{C}}{2}\left[\mathbf{u}^+(x,y) + \mathbf{u}^-(x,y)\right] + \frac{\tilde{\mathbf{C}}_n}{h}\left[\mathbf{u}^+(x,y) - \mathbf{u}^-(x,y)\right]. \tag{5}$$

The equilibrium of the third body when subjected to the external tractions $\mathbf{t}^+$ and $\mathbf{t}^-$ is guaranteed invoking the principle of virtual displacements (PVD). Let $\delta\mathbf{u}^+$, $\delta\mathbf{u}^-$ and $\delta\hat{\boldsymbol{\varepsilon}}$ be virtual displacements and strain imposed to Σ^+, Σ^- and the volume V respectively. The following PVD condition holds:

$$\int_{\Sigma^+}\mathbf{t}^{+^T}\delta\mathbf{u}^+ d\Sigma + \int_{\Sigma^-}\mathbf{t}^{-^T}\delta\mathbf{u}^- d\Sigma = \int_V \boldsymbol{\sigma}^T\delta\hat{\boldsymbol{\varepsilon}}\,dV = h\int_\Sigma \boldsymbol{\sigma}^T\delta\hat{\boldsymbol{\varepsilon}}\,d\Sigma, \tag{6}$$

with $\boldsymbol{\sigma}$ the stress vector.
Taking account of Eq. (5), the last integral in Eq. (6) can be replaced by:

$$\int_{\Sigma} \boldsymbol{\sigma}^T \delta\hat{\boldsymbol{\varepsilon}}\, d\Sigma = \frac{1}{2}\int_{\Sigma} \boldsymbol{\sigma}^T \mathbf{C}\left[\delta\mathbf{u}^+ + \delta\mathbf{u}^-\right] d\Sigma + \\ + \frac{1}{h}\int_{\Sigma} \boldsymbol{\sigma}^T \tilde{\mathbf{C}}_n \left[\delta\mathbf{u}^+ - \delta\mathbf{u}^-\right] d\Sigma. \quad (7)$$

Integrating by parts the first of the two integrals in Eq. (7) right hand side we have:

$$\int_{\Sigma} \boldsymbol{\sigma}^T \mathbf{C}\left[\delta\mathbf{u}^+ + \delta\mathbf{u}^-\right] d\Sigma = \int_{\Gamma} \left(\mathbf{C}_n^T\boldsymbol{\sigma}\right)^T \left[\delta\mathbf{u}^+ + \delta\mathbf{u}^-\right] d\Gamma + \\ - \int_{\Sigma} \left(\mathbf{C}^T\boldsymbol{\sigma}\right)^T \left[\delta\mathbf{u}^+ + \delta\mathbf{u}^-\right] d\Sigma, \quad (8)$$

where Γ represents the perimeter of the middle plane Σ, while $\mathbf{C}_n$ is the compatibility matrix depending on the normal vector at boundary. Assuming that $\Sigma^+ = \Sigma^- = \Sigma$, we can finally rewrite the PVD condition as:

$$\int_{\Sigma^+} \left[\mathbf{t}^+ - \tilde{\mathbf{C}}_n^T\boldsymbol{\sigma} + \frac{h}{2}\mathbf{C}^T\boldsymbol{\sigma}\right]^T \delta\mathbf{u}^+ d\Sigma + \int_{\Sigma^-} \left[\mathbf{t}^- + \tilde{\mathbf{C}}_n^T\boldsymbol{\sigma} + \frac{h}{2}\mathbf{C}^T\boldsymbol{\sigma}\right]^T \delta\mathbf{u}^- d\Sigma + \\ - \int_{\Gamma} \frac{h}{2}\left(\mathbf{C}_n^T\boldsymbol{\sigma}\right)^T \left[\delta\mathbf{u}^+ + \delta\mathbf{u}^-\right] d\Gamma = 0. \quad (9)$$

Since the PVD holds for any virtual displacement fields $\delta\mathbf{u}^+$ and $\delta\mathbf{u}^-$, the following equilibrium conditions are derived at the interphase:

$$\mathbf{t}^+ - \tilde{\mathbf{C}}_n^T\boldsymbol{\sigma} + \frac{h}{2}\mathbf{C}^T\boldsymbol{\sigma} = \mathbf{0} \qquad on\ \Sigma^+, \quad (10a)$$

$$\mathbf{t}^- + \tilde{\mathbf{C}}_n^T\boldsymbol{\sigma} + \frac{h}{2}\mathbf{C}^T\boldsymbol{\sigma} = \mathbf{0} \qquad on\ \Sigma^-, \quad (10b)$$

$$\mathbf{C}_n^T\boldsymbol{\sigma} = \mathbf{0} \qquad on\ \Gamma. \quad (10c)$$

3 Thermodynamic formulation of the interphase constitutive model

Looking at Fig. 1, inelasticity can take place on Σ^+ due to the intensities of $\mathbf{t}^+$ tractions, on Σ^- due to the intensities of $\mathbf{t}^-$ tractions, on Σ due to the stress state $\boldsymbol{\sigma}$ in the joint. While at the physical interfaces Σ^+ and Σ^- inelasticity is related to loss of cohesion and adhesion, in the bulk volume inelasticity can have a plastic nature, a damaging nature or a combination of both [11]. For the sake of simplicity, in this work only plasticity taking place on Σ^+ and/or on Σ^- is considered. The Helmholtz free potential energy can therefore be written, in its most general form, as:

$$\Psi\left(\hat{\boldsymbol{\varepsilon}}^e, \xi^{p+}, \xi^{p-}\right) = \frac{1}{2}\hat{\boldsymbol{\varepsilon}}^{e^T}\mathbf{E}\,\hat{\boldsymbol{\varepsilon}}^e + \Psi^{p+}\left(\xi^{p+}\right) + \Psi^{p-}\left(\xi^{p-}\right), \quad (11)$$

where $\hat{\varepsilon}^e$ is the elastic contribute of the strain at the interphase, under the hypothesis of additive decomposition of the total strain in an elastic and a plastic part:

$$\hat{\varepsilon} = \hat{\varepsilon}^e + \hat{\varepsilon}^p, \tag{12}$$

while ξ^{p+} and ξ^{p-} are two plastic internal variables. $\hat{\varepsilon}^p$ is a vector for this model having a null component on the x direction. $\mathbf{E}$ is the elasticity matrix.
The two intrinsic free energies Ψ^{p+} and Ψ^{p-} are given here in the following simple explicit expressions:

$$\Psi^{p+}\left(\xi^{p+}\right) = \frac{1}{2} h^{p+} \xi^{p+^2} \tag{13a}$$

$$\Psi^{p-}\left(\xi^{p-}\right) = \frac{1}{2} h^{p-} \xi^{p-^2}, \tag{13b}$$

with h^{p+} and h^{p-} two material constants regulating plasticity evolution.
In order to derive the interphase constitutive equations, the second principle of Thermodynamics is invoked, according to which any real mechanical process produces an increment of the total entropy. If the first principle of Thermodynamics is also considered (energy balance equation), it follows that both principles are respected if the Clausius-Duhem inequality is valid. For small displacements and isothermal purely mechanical evolutive processes, this inequality is written as

$$D = \boldsymbol{\sigma}^T \dot{\hat{\varepsilon}} - \dot{\Psi} \geq 0 \tag{14}$$

where D is the intrinsic dissipation or entropy production at the interphase and the dot refers to the derivative with respect to time of the correspondent quantity. In this particular case the dissipation can be rewritten as:

$$D = \boldsymbol{\sigma}^T \dot{\hat{\varepsilon}}^p - \chi^{p+} \dot{\xi}^{p+} - \chi^{p-} \dot{\xi}^{p-} \geq 0, \tag{15}$$

where the following positions are made:

$$\boldsymbol{\sigma} = \mathbf{E}\, \hat{\varepsilon}^e \tag{16}$$

$$\chi^{p+} = h^{p+} \xi^{p+} \tag{17}$$

$$\chi^{p-} = h^{p-} \xi^{p-}. \tag{18}$$

The onset and evolution of irreversible phenomena at the interphase are governed by plastic limit conditions. A convex Mohr-Coulomb bilinear limit surface with a tension cut-off (Fig. 2) is assumed for the physical interfaces. This convex limit domain can be expressed in the stress space using the inequalities

$$\phi^{p_1+} = \left|\mathbf{s}^{+^T}\mathbf{t}^+\right| + \left(\mathbf{n}^{+^T}\mathbf{t}^+\right) tan\varphi^+ - c_0^+\left(1-\chi^{p+}\right) \leq 0 \tag{19}$$

$$\phi^{p_2+} = \left(\mathbf{n}^{+^T}\mathbf{t}^+\right) - \sigma_0^+\left(1-\chi^{p+}\right) \leq 0 \tag{20}$$

for the Σ^+ interface, and

$$\phi^{p_1-} = \left|\mathbf{s}^{-^T}\mathbf{t}^-\right| + \left(\mathbf{n}^{-^T}\mathbf{t}^-\right) tan\varphi^- - c_0^-\left(1-\chi^{p-}\right) \leq 0 \tag{21}$$

$$\phi^{p_2-} = \left(\mathbf{n}^{-^T}\mathbf{t}^-\right) - \sigma_0^-\left(1-\chi^{p-}\right) \leq 0 \tag{22}$$

for the Σ^- interface. c_0 and σ_0 symbols have the meaning of cohesion and adhesion strengths respectively. φ represents the frictional angle.
For each interface, four cases can be distinguished:

1. elastic case: $\phi^{p_1} < 0, \quad \phi^{p_2} < 0;$
2. simple plasticity in shear: $\phi^{p_1} = 0, \quad \phi^{p_2} < 0;$
3. simple plasticity in tension: $\phi^{p_1} < 0, \quad \phi^{p_2} = 0;$
4. corner plasticity case: $\phi^{p_1} = 0, \quad \phi^{p_2} = 0.$

Once any irreversible phenomenon occurs, the principle of maximum dissipation must be applied, subjected to the conditions (19-22). Exploiting the Lagrangian method, the following function is firstly built:

$$L = D - \dot{\lambda}^{p_1+}\,\phi^{p_1+} - \dot{\lambda}^{p_2+}\,\phi^{p_2+} - \dot{\lambda}^{p_1-}\,\phi^{p_1-} - \dot{\lambda}^{p_2-}\,\phi^{p_2-}, \tag{23}$$

where $\dot{\lambda}^{p_1}$ and $\dot{\lambda}^{p_2}$ are plastic lagrangian multipliers. Then, the stationariety of the Lagrangian with respect to the mechanical variables is looked for:

$$\frac{\partial L}{\partial \boldsymbol{\sigma}} = \dot{\hat{\boldsymbol{\varepsilon}}}^{p} - \dot{\lambda}^{p_1+}\frac{\partial \phi^{p_1+}}{\partial \boldsymbol{\sigma}} - \dot{\lambda}^{p_2+}\frac{\partial \phi^{p_2+}}{\partial \boldsymbol{\sigma}} - \dot{\lambda}^{p_1-}\frac{\partial \phi^{p_1-}}{\partial \boldsymbol{\sigma}} - \dot{\lambda}^{p_2-}\frac{\partial \phi^{p_2-}}{\partial \boldsymbol{\sigma}} = 0, \tag{24}$$

$$\frac{\partial L}{\partial \chi^{p+}} = -\dot{\xi}^{p+} - c_0^{+}\dot{\lambda}^{p_1+} - \sigma_0^{+}\dot{\lambda}^{p_2+} = 0, \tag{25}$$

$$\frac{\partial L}{\partial \chi^{p-}} = -\dot{\xi}^{p-} - c_0^{-}\dot{\lambda}^{p_1-} - \sigma_0^{-}\dot{\lambda}^{p_2-} = 0. \tag{26}$$

Including Eqs. (10a-b) in Eqs. (19-22) for a plane stress condition case, Eq. (24) can be explicitly separated in:

$$\frac{\partial L}{\partial \sigma_x} = \dot{\varepsilon}_x^{p} - \dot{\lambda}^{p_1+}\left(-\frac{h}{2}\frac{\partial}{\partial \sigma_x}\frac{\partial \sigma_x}{\partial x}\right) Sign\left(t_x^{+}\right) - \dot{\lambda}^{p_1-}\left(\frac{h}{2}\frac{\partial}{\partial \sigma_x}\frac{\partial \sigma_x}{\partial x}\right) Sign\left(-t_x^{-}\right) = 0 \tag{27}$$

$$\frac{\partial L}{\partial \sigma_z} = \dot{\varepsilon}_z^{p} - \dot{\lambda}^{p_1+} tan\varphi^{+} - \dot{\lambda}^{p_2+} + \dot{\lambda}^{p_1-} tan\varphi^{-} + \dot{\lambda}^{p_2-} = 0 \tag{28}$$

$$\frac{\partial L}{\partial \tau_{xz}} = \dot{\hat{\gamma}}_{xz}^{p} - \dot{\lambda}^{p_1+} Sign\left(t_x^{+}\right) - \dot{\lambda}^{p_2+}\left(-\frac{h}{2}\frac{\partial}{\partial \tau_{xz}}\frac{\partial \tau_{xz}}{\partial x}\right) + \\ + \dot{\lambda}^{p_1-} Sign\left(-t_x^{-}\right) - \dot{\lambda}^{p_2-}\left(\frac{h}{2}\frac{\partial}{\partial \tau_{xz}}\frac{\partial \tau_{xz}}{\partial x}\right) = 0, \tag{29}$$

where $\hat{\varepsilon}_x^{p}$, $\hat{\varepsilon}_z^{p}$ and $\hat{\gamma}_{xz}^{p}$ are the components of the vector $\hat{\boldsymbol{\varepsilon}}^{p}$. t_x^{+} and t_x^{-} represent the projections of $\mathbf{t}^{+}$ and $\mathbf{t}^{-}$ tractions along $\mathbf{s}^{+}$ and $\mathbf{s}^{-}$ directions respectively. By virtue of the Schwartz's theorem, the symmetry of the second derivatives brings to:

$$\frac{\partial}{\partial \sigma_x}\left(\frac{\partial \sigma_x}{\partial x}\right) = \frac{\partial}{\partial x}\left(\frac{\partial \sigma_x}{\partial \sigma_x}\right) = 0, \tag{30a}$$

$$\frac{\partial}{\partial \tau_{xz}}\left(\frac{\partial \tau_{xz}}{\partial x}\right) = \frac{\partial}{\partial x}\left(\frac{\partial \tau_{xz}}{\partial \tau_{xz}}\right) = 0, \tag{30b}$$

which permit to conclude that

$$\dot{\varepsilon}_x^{p} = 0, \tag{31}$$

$$\dot{\varepsilon}_z^{p} = \dot{\lambda}^{p_1+} tan\varphi^{+} + \dot{\lambda}^{p_2+} - \dot{\lambda}^{p_1-} tan\varphi^{-} - \dot{\lambda}^{p_2-}, \tag{32}$$

$$\dot{\gamma}_{xz}^{p} = \dot{\lambda}^{p_1+} Sign\left(t_x^{+}\right) - \dot{\lambda}^{p_1-} Sign\left(-t_x^{-}\right), \tag{33}$$

$$\dot{\xi}^{p+} = -c_0^{+}\dot{\lambda}^{p_1+} - \sigma_0^{+}\dot{\lambda}^{p_2+}, \tag{34}$$

$$\dot{\xi}^{p-} = -c_0^- \dot{\lambda}^{p_1-} - \sigma_0^- \dot{\lambda}^{p_2-}. \tag{35}$$

Eqs. (31-35) correspond to the flow rules of the interphase written in rate form, and can be applied only if the following loading and unloading conditions hold:

$$\phi^{p_i+} \leq 0 \qquad \dot{\lambda}^{p_i+} \geq 0 \qquad \dot{\lambda}^{p_i+}\phi^{p_i+} = 0 \qquad \dot{\lambda}^{p_i+}\dot{\phi}^{p_i+} = 0, \tag{36a}$$

$$\phi^{p_i-} \leq 0 \qquad \dot{\lambda}^{p_i-} \geq 0 \qquad \dot{\lambda}^{p_i-}\phi^{p_i-} = 0 \qquad \dot{\lambda}^{p_i-}\dot{\phi}^{p_i-} = 0, \tag{36b}$$

being $i = 1, 2$.
Mixing Eqs. (34-35) and Eqs. (17-18), it is clear that h^{p+} and h^{p-} must assume negative values in order to obtain an elastic-plastic behavior with softening.
To incorporate the dilatancy effect in the model, the evolution of plasticity has to be determined assuming a non-associative case. The non-associative plastic potentials could be chosen formally equal to the limit conditions ϕ^{p_1+} and ϕ^{p_1-}, with the frictional angles replaced by the dilatancy angles δ^+ and δ^- respectively ([11, 15, 36]). Therefore, Eq. (32) should be substituted by:

$$\dot{\varepsilon}_z^p = \dot{\lambda}^{p_1+} tan\left(\delta^+\right) + \dot{\lambda}^{p_2+} - \dot{\lambda}^{p_1-} tan\left(\delta^-\right) - \dot{\lambda}^{p_2-}. \tag{37}$$

4 Discrete formulation of the constitutive model.

In order to comply with a finite element environment, it is necessary to proceed with a time-discretization of the constitutive model.
Let us assume that all the kinematic variables are known at the time $t_n \subset [0,\, T] \in \Re$, with T the overall duration of the analysis:

$\left\{\hat{\boldsymbol{\varepsilon}}_n^e, \xi_n^{p+}, \xi_n^{p-}\right\}$ assigned at t_n.

The knowledge of these variables permits to evaluate the correspondent mechanical quantities at the same instant t_n.
The goal is now to update all the kinematic and mechanical variables at instant $t_{n+1} = t_n + \Delta t$, as a result of an increment $\Delta\hat{\boldsymbol{\varepsilon}}$ of the interphase total strain. Employing an implicit backward-Euler integration procedure, the updated variables are evaluated as:

$$\hat{\boldsymbol{\varepsilon}}_{n+1}^e = \hat{\boldsymbol{\varepsilon}}_n + \Delta\hat{\boldsymbol{\varepsilon}} - \hat{\boldsymbol{\varepsilon}}_n^p - \Delta\hat{\boldsymbol{\varepsilon}}^p, \tag{38}$$

$$\xi_{n+1}^{p+} = \xi_n^{p+} + \Delta\xi^{p+}, \tag{39}$$

$$\xi_{n+1}^{p-} = \xi_n^{p-} + \Delta\xi^{p-}, \tag{40}$$

where

$$\Delta\hat{\boldsymbol{\varepsilon}}^p = \begin{bmatrix} \Delta\hat{\varepsilon}_x^p \\ \Delta\hat{\varepsilon}_x^p \\ \Delta\hat{\gamma}_{xz}^p \end{bmatrix} = \begin{bmatrix} 0 \\ \Delta\lambda^{p_1+} tan\left(\varphi^+\right) + \Delta\lambda^{p_2+} - \Delta\lambda^{p_1-} tan\left(\varphi^-\right) - \Delta\lambda^{p_2-} \\ \Delta\lambda^{p_1+} Sign\left(t_x^+\right)_{n+1} - \Delta\lambda^{p_1-} Sign\left(-t_x^-\right)_{n+1} \end{bmatrix}, \tag{41}$$

$$\Delta\xi^{p+} = -c_0^+ \Delta\lambda^{p_1+} - \sigma_0^+ \Delta\lambda^{p_2+}, \tag{42}$$

$$\Delta\xi^{p-} = -c_0^- \Delta\lambda^{p_1-} - \sigma_0^- \Delta\lambda^{p_2-}. \tag{43}$$

At each time step, the numerical procedure starts with an elastic trial predictor stage, eventually followed by a plastic corrector stage.

In the elastic predictor stage (trial quantities) all the plastic kinematic variables are kept equal to the values of the previous converged step:

$$\begin{cases} \hat{\boldsymbol{\varepsilon}}_{n+1}^{p,trial} = \hat{\boldsymbol{\varepsilon}}_{n}^{p} \\ \xi_{n+1}^{p+,trial} = \xi_{n}^{p+} \\ \xi_{n+1}^{p-,trial} = \xi_{n}^{p-}. \end{cases} \tag{44}$$

The mechanical quantities are updated accordingly:

$$\sigma_{x,n+1}^{trial} = \frac{E}{1-\nu^2}\left[\hat{\varepsilon}_{x,n+1} + \nu\left(\hat{\varepsilon}_{z,n+1} - \hat{\varepsilon}_{z,n}^{p}\right)\right], \tag{45}$$

$$\sigma_{z,n+1}^{trial} = \frac{E}{1-\nu^2}\left[\hat{\varepsilon}_{z,n+1} - \hat{\varepsilon}_{z,n}^{p} + \nu\hat{\varepsilon}_{x,n+1}\right], \tag{46}$$

$$\tau_{xz,n+1}^{trial} = G\left[\hat{\gamma}_{xz,n+1} - \hat{\gamma}_{xz,n}^{p}\right], \tag{47}$$

$$t_{x,n+1}^{+,trial} = \tau_{xz,n+1}^{trial} - \frac{h}{2}\frac{\partial}{\partial x}\left(\sigma_{x,n+1}^{trial}\right), \tag{48}$$

$$t_{z,n+1}^{+,trial} = \sigma_{z,n+1}^{trial} - \frac{h}{2}\frac{\partial}{\partial x}\left(\tau_{xz,n+1}^{trial}\right), \tag{49}$$

$$t_{x,n+1}^{-,trial} = -\tau_{xz,n+1}^{trial} - \frac{h}{2}\frac{\partial}{\partial x}\left(\sigma_{x,n+1}^{trial}\right), \tag{50}$$

$$t_{z,n+1}^{-,trial} = -\sigma_{z,n+1}^{trial} - \frac{h}{2}\frac{\partial}{\partial x}\left(\tau_{xz,n+1}^{trial}\right), \tag{51}$$

$$\chi_{n+1}^{p+,trial} = \chi_{n}^{p+}, \tag{52}$$

$$\chi_{n+1}^{p-,trial} = \chi_{n}^{p-}, \tag{53}$$

with t_z^+ and t_z^- the projections of $\mathbf{t}^+$ and $\mathbf{t}^-$ along the correspondent $\mathbf{n}$ vectors, E and G the longitudinal and tangential elastic moduli, ν the Poisson's ratio.
At this point, plasticity activation is checked. If the following inequalities are contemporary satisfied:

$$\phi_{n+1}^{p_1+,trial} < 0 \qquad \phi_{n+1}^{p_2+,trial} < 0 \qquad \phi_{n+1}^{p_1-,trial} < 0 \qquad \phi_{n+1}^{p_2-,trial} < 0, \tag{54}$$

the step is purely elastic and the trial quantities can be accepted as the corrected ones for the time t_{n+1}, since they are associated to null values of plastic lagrangian multipliers. If at least one of the inequalities (54) is not satisfied, a corrector stage is performed. In this case, in order to respect the loading-unloading conditions (36), a zero value of a plastic limit condition has to be associated with the correspondent non-null plastic multiplier.
In the most complex case, a system formed by the following four non-linear equations needs to be solved:

$$\begin{aligned} \phi_{n+1}^{p_1+}\left(\Delta\lambda^{p_1+}, \Delta\lambda^{p_2+}, \Delta\lambda^{p_1-}, \Delta\lambda^{p_2-}\right) = \\ = \left|\tau_{xz,n+1}^{trial} - G\Delta\hat{\gamma}_{xz}^{p} - \frac{h}{2}\frac{\partial}{\partial x}\left(\sigma_{x,n+1}^{trial} - \frac{E\nu}{1-\nu^2}\Delta\hat{\varepsilon}_{z}^{p}\right)\right| + \\ + \left[\sigma_{z,n+1}^{trial} - \frac{E}{1-\nu^2}\Delta\hat{\varepsilon}_{z}^{p} - \frac{h}{2}\frac{\partial}{\partial x}\left(\tau_{xz,n+1}^{trial} - G\Delta\hat{\gamma}_{xz}^{p}\right)\right] tan\left(\varphi^{+}\right) + \\ - c_0^{+}\left(1 - \chi_{n+1}^{p+,trial} - h^{p+}\,\Delta\xi^{p+}\right) = 0, \end{aligned} \tag{55a}$$

$$\phi^{p_2+}_{n+1}\left(\Delta\lambda^{p_1+},\Delta\lambda^{p_2+},\Delta\lambda^{p_1-},\Delta\lambda^{p_2-}\right)=\sigma^{trial}_{z,n+1}-\frac{E}{1-\nu^2}\Delta\hat{\varepsilon}^p_z+$$
$$-\frac{h}{2}\frac{\partial}{\partial x}\left(\tau^{trial}_{xz,n+1}-G\Delta\hat{\gamma}^p_{xz}\right)-\sigma^+_0\left(1-\chi^{p+,trial}_{n+1}-h^{p+}\,\Delta\xi^{p+}\right)=0, \quad (55b)$$

$$\phi^{p_1-}_{n+1}\left(\Delta\lambda^{p_1+},\Delta\lambda^{p_2+},\Delta\lambda^{p_1-},\Delta\lambda^{p_2-}\right)=$$
$$=\left|-\tau^{trial}_{xz,n+1}+G\Delta\hat{\gamma}^p_{xz}-\frac{h}{2}\frac{\partial}{\partial x}\left(-\sigma^{trial}_{x,n+1}+\frac{E\nu}{1-\nu^2}\Delta\hat{\varepsilon}^p_z\right)\right|+$$
$$+\left[-\sigma^{trial}_{z,n+1}+\frac{E}{1-\nu^2}\Delta\hat{\varepsilon}^p_z-\frac{h}{2}\frac{\partial}{\partial x}\left(-\tau^{trial}_{xz,n+1}+G\Delta\hat{\gamma}^p_{xz}\right)\right]tan\left(\varphi^-\right)+$$
$$-c^-_0\left(1-\chi^{p-,trial}_{n+1}-h^{p-}\,\Delta\xi^{p-}\right)=0, \quad (55c)$$

$$\phi^{p_2-}_{n+1}\left(\Delta\lambda^{p_1+},\Delta\lambda^{p_2+},\Delta\lambda^{p_1-},\Delta\lambda^{p_2-}\right)=-\sigma^{trial}_{z,n+1}+\frac{E}{1-\nu^2}\Delta\hat{\varepsilon}^p_z+$$
$$-\frac{h}{2}\frac{\partial}{\partial x}\left(-\tau^{trial}_{xz,n+1}+G\Delta\hat{\gamma}^p_{xz}\right)-\sigma^-_0\left(1-\chi^{p-,trial}_{n+1}-h^{p-}\,\Delta\xi^{p-}\right)=0. \quad (55d)$$

The solution of the system in terms of the plastic multipliers is iteratively obtained through a local Newton-Raphson procedure, and permits to arrive to the correct values of the kinematic and mechanical variables at t_{n+1}.
It remains to clarify how the partial derivatives are numerically evaluated. The total strain vector at the interphase is obtained in accordance with Eq. (5). If two shape function matrices $\mathbf{N}^+$ and $\mathbf{N}^-$ are defined for the Σ^+ and Σ^- physical interfaces respectively, it is possible to interpolate the displacement fields as:

$$\mathbf{u}^+=\mathbf{N}^+\,\mathbf{S}^+\,\mathbf{U}, \quad (56a)$$

$$\mathbf{u}^-=\mathbf{N}^-\,\mathbf{S}^-\,\mathbf{U}, \quad (56b)$$

where $\mathbf{S}^+$ and $\mathbf{S}^-$ are two selectivity matrices written in order to select only the nodes on Σ^+ or Σ^- from vector $\mathbf{U}$ collecting all the nodal displacements at the interphase. Substituting into Eq. (5):

$$\hat{\boldsymbol{\varepsilon}}=\mathbf{B}\,\mathbf{U}, \quad (57)$$

with

$$\mathbf{B}=\frac{1}{2}\mathbf{C}\left[\mathbf{N}^+\mathbf{S}^+ + \mathbf{N}^-\mathbf{S}^-\right]+\frac{1}{h}\tilde{\mathbf{C}}_n\left[\mathbf{N}^+\mathbf{S}^+ - \mathbf{N}^-\mathbf{S}^-\right] \quad (58)$$

the kinematic compatibility matrix. Consequently, it is possible to evaluate $\frac{\partial\hat{\boldsymbol{\varepsilon}}}{\partial x}=\frac{\partial\mathbf{B}}{\partial x}\,\mathbf{U}$.
Since the derivatives of the plastic strains need also to be calculated, here it is made the assumption that they are fractions of the total strains. In other words, it is assumed that

$$\hat{\varepsilon}^p_z=\beta\,\hat{\varepsilon}_z, \quad (59)$$

$$\hat{\gamma}^p_{xz}=\eta\,\hat{\gamma}_{xz}, \quad (60)$$

with $\beta,\eta\leq 1$.
In a step-by-step formulation, Eqs. (59) and (60) are rewritten, at time t_{n+1}, as:

$$\hat{\varepsilon}^p_{z,n+1}=(\beta_n+\Delta\beta)\,(\hat{\varepsilon}_{z,n}+\Delta\hat{\varepsilon}_z)\,, \quad (61)$$

$$\hat{\gamma}^{p}_{xz,n+1} = (\eta_n + \Delta\eta)\ (\hat{\gamma}_{xz,n} + \Delta\hat{\gamma}_{xz})\,. \tag{62}$$

After simple mathematical manipulations, the following extra equations giving the other two unknowns $\Delta\beta$ and $\Delta\eta$ are added in the local Newton-Raphson procedure:

$$\Delta\beta = \frac{\Delta\lambda^{p_1+} tan\left(\varphi^{+}\right) + \Delta\lambda^{p_2+} - \Delta\lambda^{p_1-} tan\left(\varphi^{-}\right) - \Delta\lambda^{p_2-} - \beta_n \Delta\hat{\varepsilon_z}}{\hat{\varepsilon}_{z,n} + \Delta\hat{\varepsilon}_z}, \tag{63}$$

$$\Delta\eta = \frac{\Delta\lambda^{p_1+} Sign\left(t_x^{+}\right)_{n+1} - \Delta\lambda^{p_1-} Sign\left(-t_x^{-}\right)_{n+1} - \eta_n \Delta\hat{\gamma_{xz}}}{\hat{\gamma}_{xz,n} + \Delta\hat{\gamma}_{xz}}. \tag{64}$$

5 Single interphase FE outcomes at quadrature point.

The nonlinear behavior of the interphase element is checked, in this section, with reference to the response to single modes.
The element has four nodes and two Gauss points, and is characterized by a unitary length and a unitary thickness. The SRI method [16] is adopted for the quadrature of the element. The tests are run in controlled displacements. Figs. 3a-c show the displacements imposed to the element for the mode I test, mode II test and mixed mode test respectively. A displacement increment Δu equal to $5 \cdot 10^{-5}$ mm is considered. For each test a parametric analysis on the h^p parameter is performed, investigating the behavior with respect to the three particular values that are reported in Table 1.
In the first case (Fig. 3a) vertical displacements only are imposed to the element. The response is equal for both the two quadrature points and is reported in Fig. 4. Fig. 4a shows the vertical and horizontal stresses trend with respect to the vertical strain. Since equal displacements are imposed to nodes, no variation in the vertical stresses between two Gauss points can be detected and a null spatial derivative is returned. If zero horizontal displacements are also present, no tangential traction and stress are obtained, while the vertical traction equals the vertical stress. Fig. 4a highlights the main characteristic of an interphase element, that is the possibility to transfer horizontal stresses: this is impossible for a classic interface element. The nonlinear behavior begins when the vertical traction approaches its limit value. The softening branch is linear with a slope as higher as greater is h^p in absolute value. A zero value of the stress/traction is maintained when the element is completely damaged, correspondent to $\chi^{p+} = 1$ value in Fig. 4b. In the same Fig. 4b the trend of the β coefficient is also reported. For the specific case, it is clear how, after plasticity activation, the most of the strain increment quickly transforms in a plastic contribution, with a small dependency on the h^p parameter. This is reasonable, because it is related not only to the actual point in the descending branch, but also and more to the stiffness of the element.
In the second case (Fig. 3b), horizontal displacements only are imposed, using the same mechanical parameters adopted for the mode I test. This is a pure mode II case and only tangential contributes for traction and stress are detectable, as no gradient in the shear stress exists. The stress-strain curves at a quadrature point of the interphase element are shown in Fig. 5a. Their information is completed by the evolution of η and χ^p parameters, reported in the associated Fig. 5b. After the achievement of the cohesion strength at the interphase, stresses descend linearly

till zero. At the same time, χ^p values vary linearly till 1 while correct non-linear trend is obtained for η.
Fig. 6 shows the outcomes of the third case, when the boundary conditions imposed for modes I and II are mixed. A double vertical displacement on node 3 is considered, as in Fig. 3c. Figs. 6a and b refer to the behavior of the interphase in the z direction, Figs. 6c and d on the x direction. The results are reported for the left quadrature point. Plasticity is firstly activated for vertical tractions only (simple plasticity in tension) and evolves faster once a corner case is gotten. The overall behavior of the interphase remains unchanged with respect to the simple modes, with the only difference that the co-presence of contact tractions at the physical interface leads to higher values of plasticity.
In Fig. 4 (mode I case) and Fig. 5 (mode II case) the results on Σ^+ only are shown, because equal results are obtained for Σ^-. The situation changes in the third case, where the vertical stress gradient leads to different values of the tangential tractions and shear stresses. In Fig. 7a detail of Fig. 6c is shown. Also the trend of t_x^- intensities for varying h^{p+} $(= h^{p-})$ are included in the figure.

6 Validation of the model

To validate the interphase model through comparisons with real cases, the results of the experimental tests carried out by Portioli and Cascini [31] on two masonry panels are numerically reproduced in this section. The two wall panels are schematized in Fig. 8. They are made of bricks with dimensions of 200 x 100 x 50 mm, and dry joints. The first panel (Fig. 8a) is composed of 8 courses for a total height of 400 mm; the second panel (Fig. 8b) is instead made of 12 courses for a total height of 600 mm. They were labeled as '8C' and 12C' panels respectively. Both specimens are five-and-half bricks wide for a total length of 1100 mm. The left side of their foundation is fixed, the right side is instead movable in order to allow horizontal and vertical displacements. The support on the right is connected to a scale able to measure its total vertical reaction. Vertical displacements were experimentally imposed with increments of 1.0 mm.
In Fig. 9 a reproduction of the deformed shapes at vertical displacements equal to 20 mm (Fig. 9a) and 50 mm (Fig. 9b) is reported for the 8C panel. The same is done in Figs. 10a-b for the 12C panel. Contemporaneously, Fig. 11 plots in symbols the experimental base reaction vs the imposed vertical displacement.
For the 8C panel, an initial base reaction of 250 N was experimentally measured. Then, during the test, a progressive loss of weight was observed until the failure of the wall, reached when the base reaction was approximately equal to 104 N. A a 'stair-stepped' fracture induced by the applied displacement at the base progressively separates a bottom right triangular rigid macro-block from the rest of the panel. At 50 mm, three different parts can be identified in the wall: two rigid macro-blocks of triangular shape at the two sides, one fixed (left) and one moving (right), and a third macro-block rotating with respect to the point which separates the fixed and moving supports. The last macro-block shows diffused cracks at failure.
For the 12C panel, again three macro-blocks could be distinguished at the end of the experimental test, but the diffused cracks in the rotating macro-block are much less pronounced, thanks to the stabilizing effect furnished by the added courses.

For this panel, an initial base reaction of 375 N was obtained, monotonically decreasing till the value of 87 N at failure, when the complete detachment between the movable rigid macro-block and the rest of the wall was experimentally observed.
The numerical simulations were conducted trying to reproduce as much as possible the real configurations. Each masonry brick was discretized with two elastic quadrilateral linear elements having elastic modulus equal to 12500 MPa, Poisson's ratio 0.15, density 12.0 kN/m^3. Each block was surrounded by 6 interphase elements: two on the top, two on the bottom and one on each side of the brick. Null values of cohesion c_0, adhesion σ_0 and plastic hardening h^p were set for the interphases, in order to comply with the real condition of dry joints. The friction coefficient was chosen equal to 0.4, as suggested in [31]. In this way, a pure Coulomb friction behavior was simulated. The stiffness of the joints was derived considering the elastic modulus equal to one thousandth of that of the bricks, while same Poisson's ratio was used. Regarding the boundary conditions, the fixed part of the base was modeled by imposing null displacements for the correspondent nodes, while for the movable part only horizontal displacements were allowed. The analyses were carried out controlling the vertical displacement imposed to the movable part, with a rate of 1 mm/step according to the experimental protocol.
For the 8C panel, an initial base reaction of 240 N was found (Fig. 11), dependent on the chosen unit weight and slightly different than the experimental one. For the entire analysis the base reaction vs imposed displacement curve matches well the experimental data. Also the collapse mechanism is correctly caught: the 'stair-stepped' fracture is visible at 20 mm (Fig. 9c), as the distinction of the three macro-blocks at 50 mm (Fig. 9d), with diffused cracks in the rotating macro-block.
For the 12C panel, a base reaction of 360 N was numerically obtained at the beginning of the analysis. In this case, the reaction-displacement curve (Fig. 11) is quantitatively similar to the experimental data, but not as close as for the 8C panel. Besides, the movable macro-block at the end of the analysis is still not completely detached. However, the general judgment is positive. The reaction-displacement curve in fact crosses that one of the 8C panel as expected, and furnishes almost the same initial and final values. The diffused cracks in the wall at 50 mm (Fig. 10d) are also less visible than those of the 8C panel at the same imposed displacement, as experimentally obtained.
At the end, it is possible to conclude that the model correctly reproduced the collapse mechanisms and furnished a good approximation of the experimental base reaction-displacement curves. The meso-modeling approach is in fact able to reproduce mechanically and kinematically all the intermediate configurations. This is not possible, for example, if solving a limit analysis problem, where only the configuration at collapse can be identified.

7 A case study: the analysis of a wall in 'Baglio Granatelli' - Sicily.

7.1 Historical background and description of the structure and its materials.

The 'Baglio Granatelli' is a big complex in the territory of Mazara del Vallo (Trapani - Sicily), nearby county road 50. A lot of similar structures are present in the same site, because they were commonly used in the past for many months of

the year as residential buildings for entire families of farmers. The structure was probably built in the first years of the 18^{th} century.
In Fig. 8a an axonometric view of the complex is reported (Bianco et al. [8]), while the Est front is visible in Fig. 8b. A map of the structure is instead furnished in Fig. 8c. In these figures the wall, subject matter of this study, is enclosed in a rectangle. The 'Baglio' has an overall rectangular shape with an internal court. All around, a lot of storage rooms were present. Only one side of the structure was for residential use, and precisely the only part with two stories, close to a little tower. A chapel is also present, external to the court, as typical in the zone. The main entrance to the court was at the beginning on the opposite side with respect to the actual position. It was later modified when a new more important road was built.
The structure was totally built with masonry, with a lot of openings surrounded by natural carving stones. Two openings have a round arch and one a lowered arch, made with the same stones. The masonry blocks are constituted by calcareous tuff, a very common material along the Sicilian coasts. Mortar was obtained from a mixture of sand and lime. Wooden roofs were extensively used but also barrel and cross vaults were present. In the actual state many of the roofs collapsed. Serious damages are detectable: wind and water erosion on both blocks and ground, ground movements related to the clay nature of the soil, deterioration of wood and mortar, advanced state of abandonment.

7.2 Numerical analysis of the wall.

With the aim to apply the proposed model to a real case, part of the wall in the Est front was selected and analyzed. Attention was paid to a portion, between two transverse bearing walls, where a collapse of masonry had taken place due to a variation of the ground surface level. The vertical ground movement had imposed a vertical displacement to the base of the wall, by which a typical arc-shaped collapse happened. A picture of the actual state of the wall is shown in Fig. 13a. As visible in the picture, also the roof had collapsed in the same portion. The author of the present paper doesn't know which one of them collapsed first. A detailed survey of the wall is reported in Fig. 13b. This step is fundamental if the goal is to run a simulation on a detailed model of the structure. In our case, being concentrated more on the proposed model performance and being unknown the real arrangement in the missing part, the analysis process was divided into two steps. Starting from the real state of the structure (Fig. 13a-b), it was looked for the most regular and periodic arrangement of blocks that best matched up with the real configuration (Fig. 13c). This simplified configuration was last discretized and then analyzed. The idealization of the real structure led to the recognition of three main block sizes: 11.5×23 cm, 24×23 cm, 51×23 cm. The average mortar thickness was equal to around 2 cm. The total length of the analyzed wall was 10.51 m, its height 5.73 m, its depth 22 cm.
The finite element model (Fig. 14) was built using a total of 8999 finite elements, 5593 of which are solids elements with linear elastic behavior representing the blocks, 3406 are instead elastoplastic interphase elements representing the mortar joints. Each element has four nodes, for a total number of nodes of 9973. 2×2 Gauss points were chosen for solid elements. Zero displacements were imposed to

the vertical boundaries due to the presence of transverse walls. Also zero displacements were imposed at the two sides of the missing part. A distribution of vertical springs whose thickness changed from infinite to zero was considered as boundary condition at the base of the missing part, in order to simulate the erosion of the ground under the wall.
The specific case is recognizable as one of the most known crack patterns in masonry building on the basis of the settlement location. A good list of these cases can be found in Can et al. ([10]).
The adopted mechanical parameters are reported in Table 2. The values chosen for blocks and mortar (subscripts b and m respectively) were derived by laboratory tests not directly executed on the materials of the structure, but on blocks and mortar of the same kind. These values were already available in literature.
The analysis was conducted using one step only, without imposition of any boundary displacement or forces: from time 0 (infinite stiffness for springs) to time 1 (zero stiffness of springs) the self-weight of the bricks led to the collapse mechanism shown in Fig. 15b. At the beginning of the analysis the springs acted on the wall as if it was blocked on its entire base. As soon as the stiffness of the springs felt down to zero the program started to iterate for a total of 9264 iterations, until the value of 1.0 x 10^{-5} Ncm of relative energy was reached. At convergence, two main 'stair-stepped' fractures at the two sides appeared, connected on the top by an horizontal crack and forming a typical arc-shaped collapse (Fig. 15b), as it had happened to the wall (Fig. 15a). To better highlight the propagated fracture, it has been schematized in thicker line in Fig. 15c. Comparing the actual state of the wall and the outcome of the numerical simulation, it can be concluded that the model was able to correctly catch its collapse mechanism.

8 Conclusions

In the present work an interphase constitutive model has been formulated with the aim to simulate damages in masonry structures in the framework of a mesoscopic approach.
The model has been written following a thermodynamically consistent theory. Its discrete version has been also furnished and implemented in a research-oriented finite element program. Numerical examples on a single interphase element highlighted the main features of the constitutive behavior at the quadrature point.
With respect to the classic interface elements the model also included the effects of internal stresses. This fact, together with the possibility to identify the activation of plasticity in both the two physical interfaces, makes the model more suitable for solving real cases.
The model was validated through comparisons with experimental data available in literature: the obtained results were satisfactory and encouraged the use of the model for a real case. The model was therefore applied to solve, as a first attempt, the inverse problem for a case-study, regarding a real wall with a missing part clearly collapsed because of ground settlement. The typical arc-shaped collapse mechanism for these cases was correctly simulated by eliminating part of the constraints at the base of the wall, as an effect of its self-weight only.
Thus, it potentially could be used for all those cases where differential foundation settlements take place, better if included in a more complete model where

also the ground-structure interaction is contemplated. This step could be a future development of the model, together with more in-depth applications.

Acknowledgements

The author gratefully acknowledges Prof. Giuseppe Giambanco for the profitable discussions on the constitutive model, and Miss Milena Di Benedetto for her contribution to Fig. 13.

Funding

This work was supported by Italian Ministry for University and Research (MIUR) for PRIN-15, project No.2015LYYXA8, *Multiscale mechanical models for the design and optimization of microstructured smart materials and metamaterials.*

Compliance with Ethical Standards

Conflict of Interest: the author declares that he has no conflict of interest.

References

1. Addessi D, Sacco E (2012) A multi-scale enriched model for the analysis of masonry panels. Int J Solids Struct 49(6):865–880
2. Addessi D, Sacco E (2016) Nonlinear analysis of masonry panels using a kinematic enriched plane state formulation. Int J Solids Struct 90:194–214
3. Alessandri C, Garutti M, Mallardo V, Milani G (2015) Crack Patterns Induced by Foundation Settlements: Integrated Analysis on a Renaissance Masonry Palace in Italy. International Journal of Architectural Heritage 9(2):111–129
4. Alfano G, Sacco E (2006) Combining interface damage and friction in a cohesive-zone model. Int J Numer Meth Eng 68(5):542–582
5. Amorosi A, Boldini D, De Felice G, Malena M, Sebastianelli M (2014) Tunnelling-induced deformation and damage on historical masonry structures. Geotechnique 64(2):118–130
6. Augarde CE, Burd HJ (2001) Three-dimensional finite element analysis of lined tunnels. Int J Numer Anal Met 25(3):243–262
7. Baraldi D, Reccia E, Cecchi A (2017) In plane loaded masonry walls: DEM and FEM/DEM models. A critical review. Meccanica DOI 10.1007/s11012-017-0704-3, , in press
8. Bianco C, Bianco G, De Simone M (1987) Mazara: bagli, ville e torri fra il Mazaro e il Delia. Master's thesis, Universita' degli Studi di Palermo, Facolta' di Architettura, Dipartimento di Rappresentazione, Palermo
9. Burd HJ, Houlsby GT, Augarde CE, Liu G (2000) Modelling tunnelling-induced settlement of masonry buildings. Proceedings of the Institution of Civil Engineers - Geotechnical Engineering 143(1):17–29

10. Can E, Kuşcu Ş, Kartal ME (2012) Effects of mining subsidence on masonry buildings in Zonguldak hard coal region in Turkey. Environ Earth Sci 66(8):2503–2518
11. Fileccia Scimemi G, Giambanco G, Spada A (2014) The interphase model applied to the analysis of masonry structures. Comput Methods Appl Mech Engng 279:66–85
12. Galassi S, Paradiso M, Tempesta G (2013) Non-linear analysis of masonry structures subjected to external settlements. Open Journal of Civil Engineering 3(2A):18–26
13. Giambanco G, Fileccia Scimemi G (2006) Mixed mode failure analysis of bonded joints with rate-dependent interface models. Int J Numer Meth Eng 67(8):1160–1192
14. Giambanco G, Mróz Z (2001) The interphase model for the analysis of joints in rock masses and masonry structures. Meccanica 36(1):111–130
15. Giambanco G, Rizzo S, Spallino R (2001) Numerical analysis of masonry structures via interface models. Comput Methods Appl Mech Engng 190(49):6493–6511
16. Giambanco G, Fileccia Scimemi G, Spada A (2012) The interphase finite element. Computational Mechanics 50(3):353–366
17. Giambanco G, La Malfa Ribolla E, Spada A (2017) Meshless meso-modeling of masonry in the computational homogenization framework. Meccanica DOI 10.1007/s11012-017-0664-7, , in press
18. Giambanco G, Di Gati L (1997) A cohesive interface model for the structural mechanics of block masonry. Mechanics Research Communications 24(5):503–512
19. Giambanco G, La Malfa Ribolla E, Spada A (2014) CH of masonry materials via meshless meso-modeling. Frattura e integrita' strutturale 8(29):150–165
20. Giardina G, van de Graaf AV, Hendriks MA, Rots JG, Marini A (2013) Numerical analysis of a masonry façade subject to tunnelling-induced settlements. Eng Struct 54:234–247
21. Iannuzzo A, Angelillo M, De Chiara E, De Guglielmo F, De Serio F, Ribera F, Gesualdo A (2017) Modelling the cracks produced by settlements in masonry structures. Meccanica DOI 10.1007/s11012-017-0721-2, , in press
22. Leonetti L, Greco F, Trovalusci P, Luciano R, Masiani R (2018) A multiscale damage analysis of periodic composites using a couple-stress/Cauchy multidomain model: Application to masonry structures. Compos Part B-Eng 141:50–59
23. Liu G, Houlsby GT, Augarde CE (2000) 2-dimensional analysis of settlement damage to masonry buildings caused by tunnelling. The Structural Engineer 79(1):19–25
24. Lotfi HR, Shing PB (1994) Interface model applied to fracture of masonry structures. J Struct Eng 120(1):63–80
25. Lourenço PB, Rots JG (1997) Multisurface interface model for analysis of masonry structures. J Eng Mech 123(7):660–668
26. Marfia S, Sacco E (2012) Multiscale damage contact-friction model for periodic masonry walls. Comput Methods Appl Mech Engng 205-208:189–203
27. Massart TJ, Peerlings RHJ, Geers MGD (2007) An enhanced multi-scale approach for masonry wall computations with localization of damage. Int J Numer Meth Eng 69(5):1022–1059

28. Netzel H, van Zijl GPAG (2004) Nonlinear numerical simulation of settlement-induced damage to solid masonry walls. In: 13^{th} International Brick Masonry Conference, Amsterdam
29. Parrinello F, Failla B, Borino G (2009) Cohesive-frictional interface constitutive model. Int J Solids Struct 46(13):2680–2692
30. Petracca M, Pelà L, Rossi R, Oller S, Camata G, Spacone E (2016) Regularization of first order computational homogenization for multiscale analysis of masonry structures. Computational Mechanics 57(2):257–276
31. Portioli F, Cascini L (2016) Assessment of masonry structures subjected to foundation settlements using rigid block limit analysis. Eng Struct 113:347 – 361
32. Raffa ML, Lebon F, Rizzoni R (2017) Derivation of a model of imperfect interface with finite strains and damage by asymptotic techniques: an application to masonry structures. Meccanica DOI 10.1007/s11012-017-0765-3, , in press
33. Serpieri R, Albarella M, Sacco E (2017) A 3D microstructured cohesive-frictional interface model and its rational calibration for the analysis of masonry panels. Int J Solids Struct 122-123:110–127
34. Smoljanović H, Nikolić Ž, Živaljić N (2015) A combined finite-discrete numerical model for analysis of masonry structures. Eng Fract Mech 136:1–14
35. Son M, Cording EJ (2008) Numerical model tests of building response to excavation-induced ground movements. Canad Geotech J 45(11):1611–1621
36. Spada A, Giambanco G, Rizzo P (2009) Damage and plasticity at the interfaces in composite materials and structures. Comput Methods Appl Mech Engng 198(49):3884–3901
37. Spada A, Giambanco G, La Malfa Ribolla E (2015) A FE-meshless multiscale approach for masonry materials. Procedia Engineering 109:364–371
38. Truong-Hong L, Laefer DF (2013) Impact of modeling architectural detailing for predicting unreinforced masonry response to subsidence. Automat Constr 30:191–204

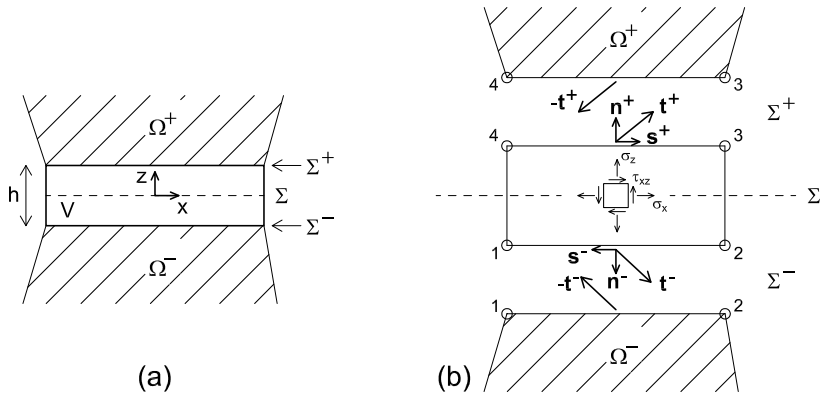

Fig. 1 $x-z$ view of (a) a weak joint of thickness h and volume V between two adherents Ω^+ and Ω^-; (b) schematic representation of the interphase element and its mechanical variables.

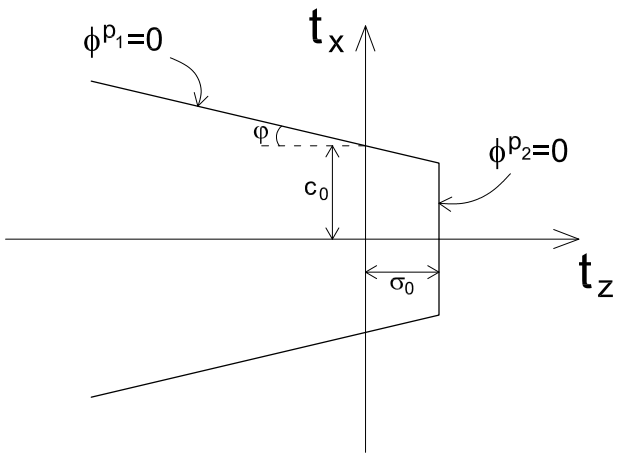

Fig. 2 Bi-linear Mohr-Coulomb with tension cut-off activation domain.

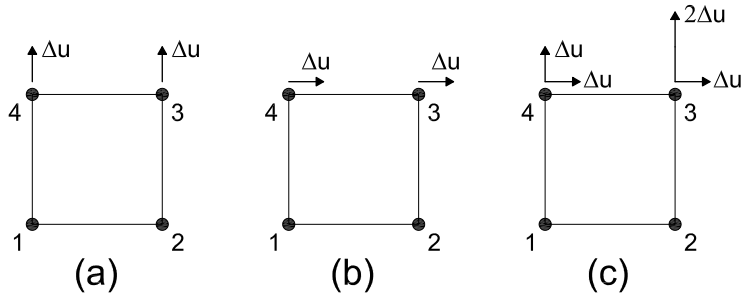

Fig. 3 Boundary conditions on the interphase finite element nodes in case of: (a) simple mode I test; (b) simple mode II test; (c) mixed mode test. $\Delta\mathbf{u} = 5 \cdot 10^{-5}\, mm$

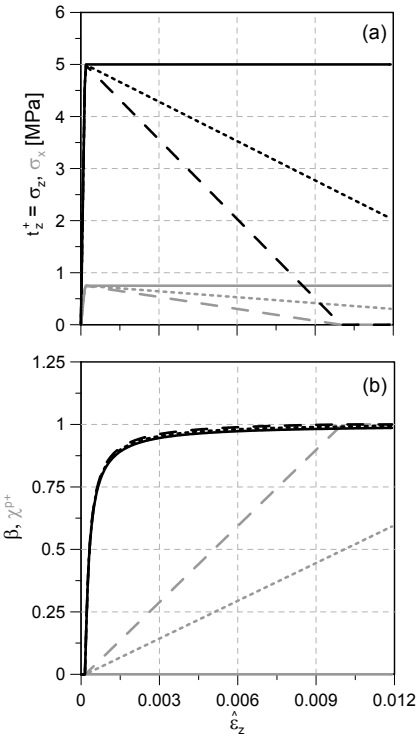

Fig. 4 Mode I response: (a) stress-strain curves; (b) $\beta - \hat{\varepsilon}_z$ and $\chi^{p+} - \hat{\varepsilon}_z$ curves. Continuous lines: $h^{p+} = 0\, MPa^{-1}$; dotted lines: $h^{p+} = -10\, MPa^{-10}$; dashed lines: $h^{p+} = -20\, MPa^{-1}$.

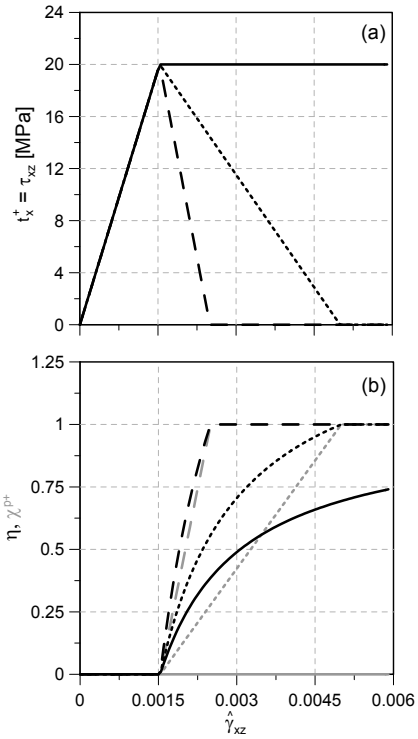

Fig. 5 Mode II response: (a) stress-strain curves; (b) $\eta - \hat{\gamma}_{xz}$ and $\chi^{p+} - \hat{\gamma}_{xz}$ curves. Continuous lines: $h^{p+} = 0\, MPa^{-1}$; dotted lines: $h^{p+} = -10\, MPa^{-1}$; dashed lines: $h^{p+} = -20\, MPa^{-1}$.

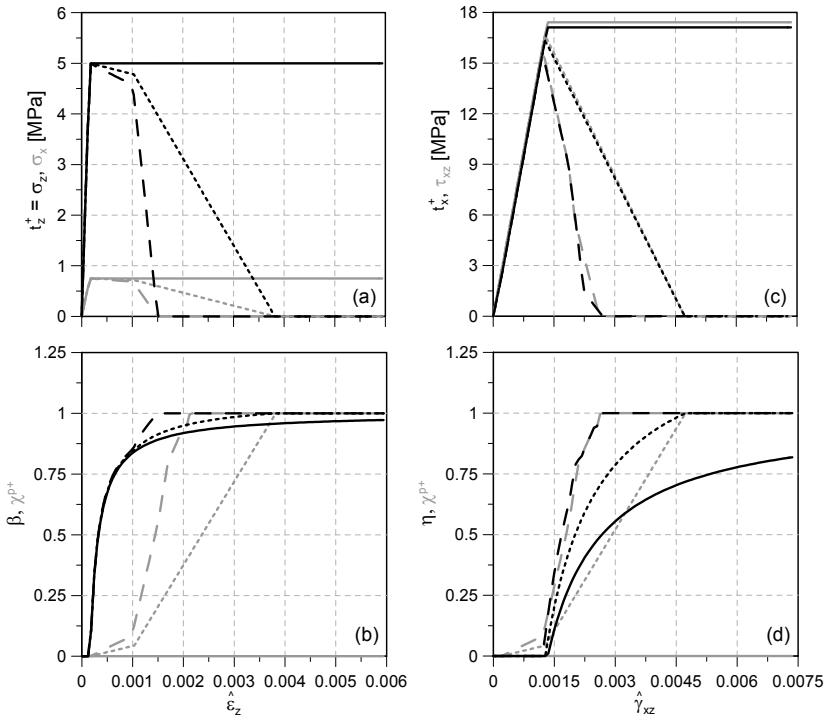

Fig. 6 Mixed mode response: (a) stress-strain curves with respect to $\hat{\varepsilon}_z$; (b) $\beta - \hat{\varepsilon}_z$ and $\chi^{p+} - \hat{\varepsilon}_z$ curves; (c) stress-strain curves with respect to $\hat{\gamma}_{xz}$; (d) $\eta - \hat{\gamma}_{xz}$ and $\chi^{p+} - \hat{\gamma}_{xz}$ curves. Continuous lines: $h^{p+} = 0\,MPa^{-1}$; dotted lines: $h^{p+} = -10\,MPa^{-1}$; dashed lines: $h^{p+} = -20\,MPa^{-1}$.

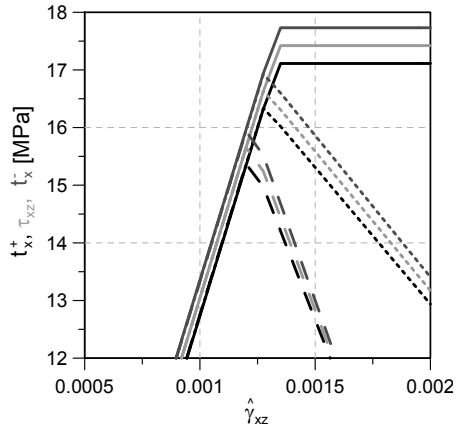

Fig. 7 Mixed mode response. A detail of: $t_x^+ - \hat{\gamma}_{xz}$ curves (black lines), $\tau_{xz} - \hat{\gamma}_{xz}$ curves (40 % black lines), $t_x^- - \hat{\gamma}_{xz}$ curves (70 % black lines). Continuous lines: $h^{p+} = 0\, MPa^{-1}$; dotted lines: $h^{p+} = -10\, MPa^{-1}$; dashed lines: $h^{p+} = -20\, MPa^{-1}$.

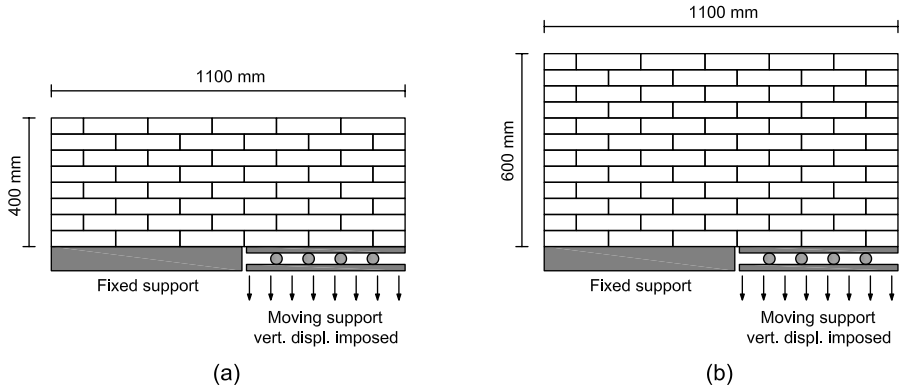

Fig. 8 Geometry and boundary conditions for the experimental panels tested by Portioli and Cascini [31]. (a) 8C panel; (b) 12C panel.

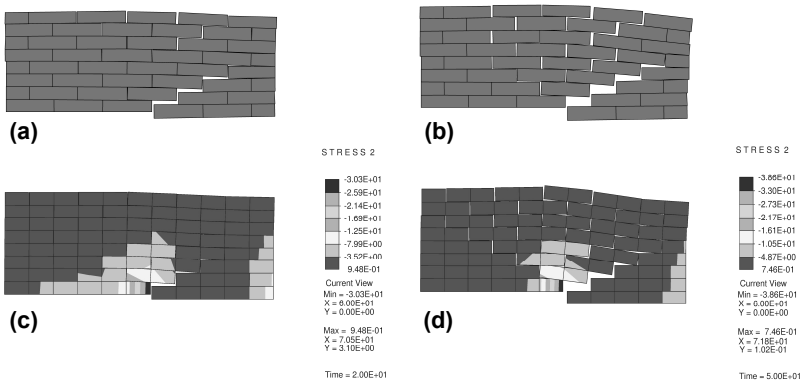

Fig. 9 Reproduction of the experimental deformed shapes obtained by Portioli and Cascini [31] for the 8C panel, at vertical settlement equal to (a) 20 mm and (b) 50 mm. Numerical results at (c) 20 mm and (v) 50 mm.

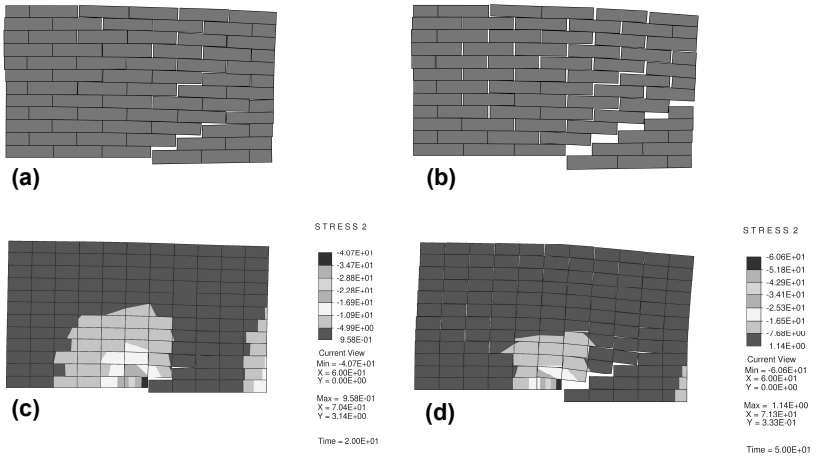

Fig. 10 Reproduction of the experimental deformed shapes obtained by Portioli and Cascini [31] for the 12C panel, at vertical settlement equal to (a) 20 mm and (b) 50 mm. Numerical results at (c) 20 mm and (v) 50 mm.

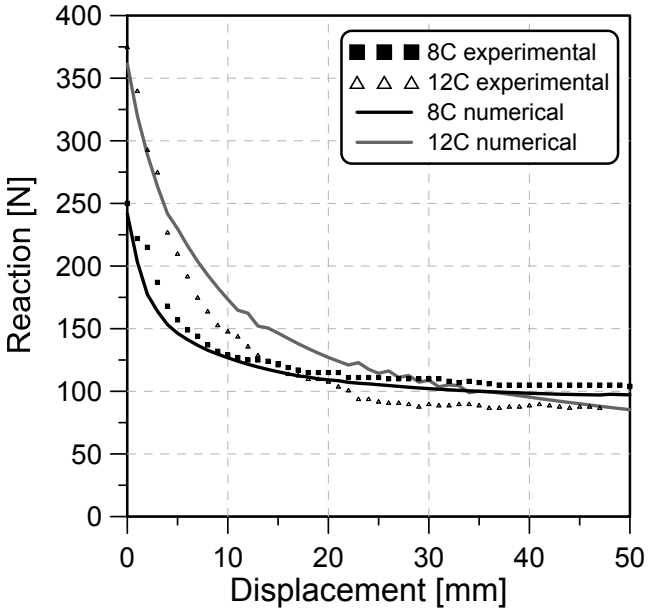

Fig. 11 Base reaction vs imposed displacement curves.

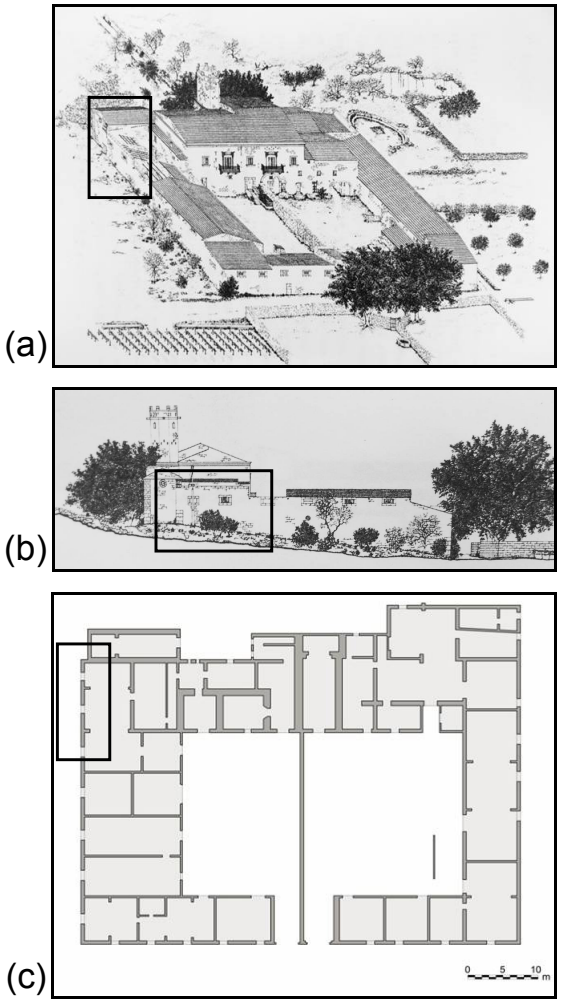

Fig. 12 'Baglio Granatelli' - Mazara del Vallo (Sicily, Italy). (a) Axonometric view, (b) frontal projection and (c) map [8] with location of the analyzed wall.

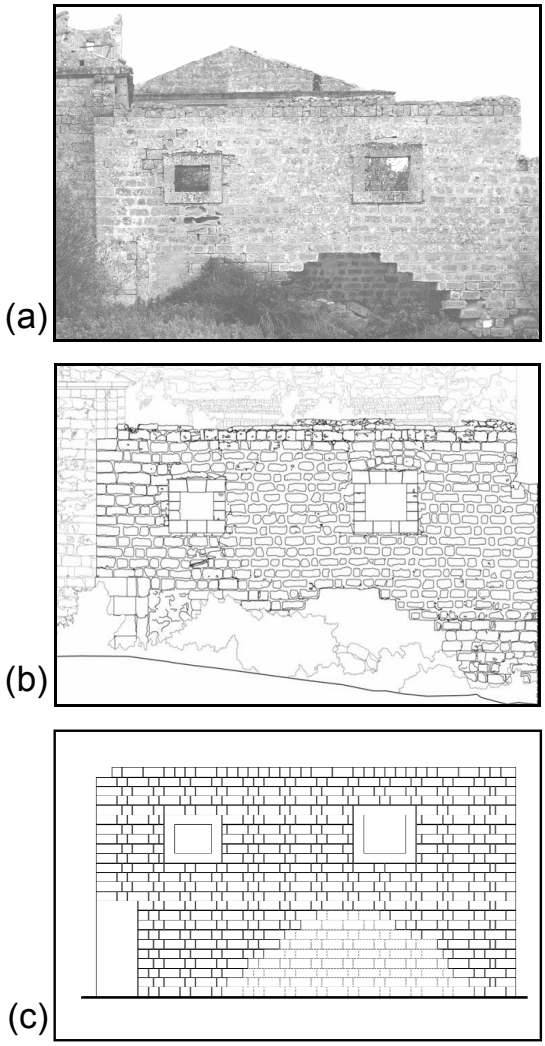

Fig. 13 'Baglio Granatelli' - Mazara del Vallo (Sicily, Italy). (a) A picture of the actual state, (b) detailed survey of the wall, (c) idealization of the best regular configuration.

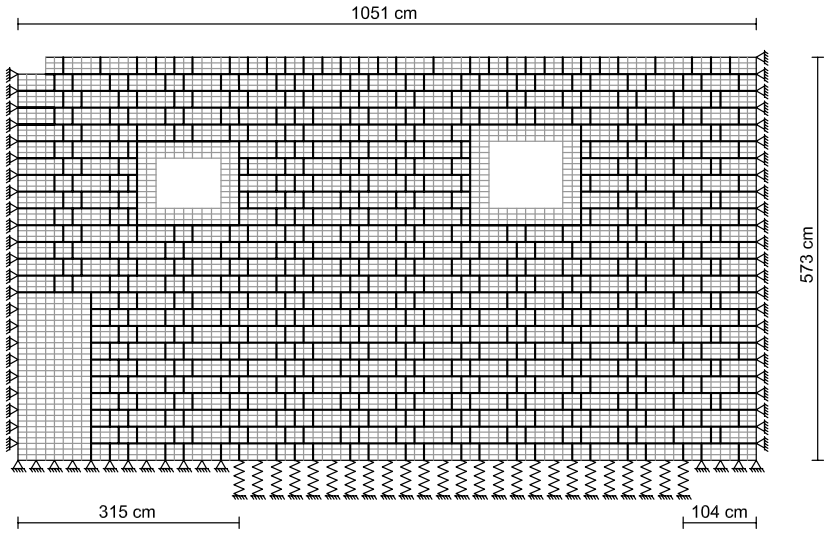

Fig. 14 Case-study: FE discretization of the wall with indication of boundary conditions (thicker lines are interphases).

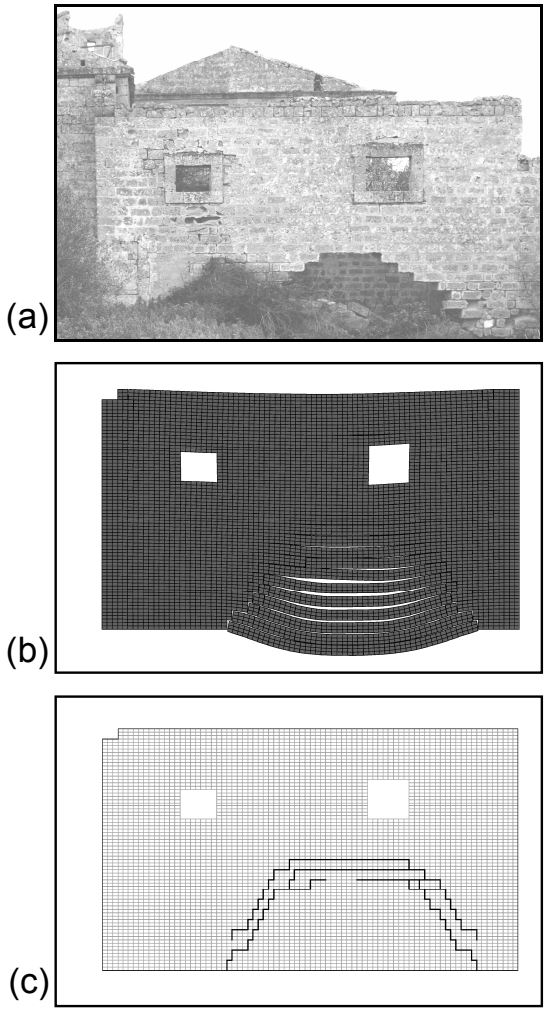

Fig. 15 Case-study: comparisons between (a) real state and (b-c) numerical outcomes (Deformed shape in (b) amplified by a factor of 2000).

E $[MPa]$	ν	$h^{p+} = h^{p-}$ $[MPa]^{-1}$	$\varphi^+ = \varphi^-$ $[^\circ]$	$c_0^+ = c_0^-$ $[MPa]$	$\sigma_0^+ = \sigma_0^-$ $[MPa]$
30000	0.15	0	30	20	5
		-10			
		-20			

Table 1 Material mechanical parameters adopted for the single interphase element response.

E_b $[MPa]$	ν_b	ρ_b $[kg/m^3]$	E_m $[MPa]$	ν_m	$\varphi^+ = \varphi^-$ $[^\circ]$	$h^{p+} = h^{p-}$ $[MPa]^{-1}$	$c_0^+ = c_0^-$ $[MPa]$	$\sigma_0^+ = \sigma_0^-$ $[MPa]$	joint
10142	0.2	$1.6{\cdot}10^3$	8000	0.15	35	-1000	$1.8{\cdot}10^{-2}$	$0.4{\cdot}10^{-2}$	bed
						-10000	$0.3{\cdot}10^{-2}$	$0.1{\cdot}10^{-2}$	head

Table 2 Material mechanical parameters adopted for the 'Baglio Granatelli' wall.